Ceramics International xxx (xxxx) xxx–xxx

Contents lists available at ScienceDirect

Ceramics International

journal homepage: www.elsevier.com/locate/ceramint

# In situ synthesis of visible-light-driven Z-scheme AgI/$Bi_2WO_6$ heterojunction photocatalysts with enhanced photocatalytic activity

Wenjing Xue[a], Zhiwei Peng[b,c], Danlian Huang[a,c,*], Guangming Zeng[a,c,*], Xiaoju Wen[a,c], Rui Deng[a,c], Yang Yang[a,c], Xuelei Yan[a,c]

[a] College of Environmental Science and Engineering, Hunan University, Changsha 410082, PR China
[b] Zoomlion Heavy Industry Science and Technology Co.,Ltd, Changsha 410013, PR China
[c] Key Laboratory of Environmental Biology and Pollution Control (Hunan University), Ministry of Education, Hunan University, Changsha 410082, PR China

ARTICLE INFO

*Keywords:*
Photocatalysis
AgI/$Bi_2WO_6$
Heterojunction
Z-scheme
Tetracycline

ABSTRACT

In this work, an efficient visible-light-response AgI/$Bi_2WO_6$ heterojunction was successfully prepared via in situ precipitation of AgI nanoparticles on the aligned nanosheets of three-dimensional $Bi_2WO_6$ hierarchical microspheres for the first time. Studies suggested that the AgI/$Bi_2WO_6$ heterojunction exhibited excellent photocatalytic activity for tetracycline (TC) degradation compared to pure $Bi_2WO_6$ and AgI under visible light irradiation. Doping 20 wt% AgI resulted in the optimal TC photodegradation rate, which was 5.4 and 3.3 times higher than pure $Bi_2WO_6$ and AgI, respectively. The high-resolution transmission electron microscopy (HRTEM), X-ray diffraction (XRD), and X-ray photoelectron spectroscopy (XPS) verified that Ag nanoparticles generated on AgI/$Bi_2WO_6$ heterojunction surface in photocatalytic degradation process, which was beneficial for promoting the rapid combination of electrons on the conduction band of $Bi_2WO_6$ with the holes on the valence band of AgI and the separation and transfer of photogenerated electron-hole pairs. Accordingly, the nontraditional transport pathway of photogenerated electrons and holes based on the Z-scheme system that consisted of $Bi_2WO_6$, AgI, and Ag was confirmed. Based on the systematic experimental evidence, the possible enhanced photocatalytic mechanism was proposed.

## 1. Introduction

Over the past several decades, the growing environmental pollution and energy crisis have gained much concern to harnessing solar energy [1–4]. Semiconductor photocatalysis was proven to be a green economy and promising technology to solve the aforementioned issues [5]. However, traditional semiconductor photocatalyst such as $TiO_2$ only can utilize ultra-violet light which just makes up 4% of solar light [6,7]. Thus in order to exploit the solar light to maximum, developing new-type and efficient visible light driven (VLD) photocatalysts is still necessary.

Nowadays, bismuth-based semiconductors have attracted much interests as an efficient VLD photocatalysts [8–10]. Among them, $Bi_2WO_6$ (bandgap: 2.60–2.80 eV) has become a promising photocatalyst owing to its low expense, nontoxicity, good chemical stability and photocatalytic activity [11,12]. Nevertheless, pure $Bi_2WO_6$ still has a poor photocatalytic activity because of its unsatisfactory light absorption and quick recombination of photogenerated electrons and holes [13,14]. Therefore, many methods have been developed to enhance the photocatalytic properties of $Bi_2WO_6$, such as doping metals [15], constructing heterojunctions and so on [9,16]. Up to now, construction of $Bi_2WO_6$-based heterojunctions is verified as an effective and constructive strategy [17–21]. Silver halides (AgX) have been adopted as a photosensitive material in photographic field. Previous studies have shown that the AgX-based photocatalysts exhibited excellent catalytic activity in the photo-oxidation of organic pollutants [22,23]. However, pure AgI presents irregular spherical particles and is easy to agglomerate thus leading to unfavorable photocatalytic performance. Studies have shown that a proper substrate can readily disperse AgX even reduce its particle size in favor of the formation of heterojunction, which further improves the stability and photoactivity of pure AgX [24,25]. As one of AgX, AgI can also respond to visible light with a narrow band gap [24]. The valence band of $Bi_2WO_6$ (+3.21 eV) is less negative than the valence band of AgI (+2.36 eV) [25], which accelerates the separation of photogenerated carriers. Moreover, the morphology of semiconductor has a certain effect on its photocatalytic properties. It has been proved that the three-dimensional (3D) $Bi_2WO_6$ hierarchical microspheres structure possess a high surface area, which favors a better

* Corresponding authors at: College of Environmental Science and Engineering, Hunan University, Changsha 410082, PR China
*E-mail addresses:* huangdanlian@hnu.edu.cn (D. Huang), zgming@hnu.edu.cn (G. Zeng).

https://doi.org/10.1016/j.ceramint.2018.12.119
Received 11 November 2018; Received in revised form 16 December 2018; Accepted 17 December 2018

degradation ability and also restrain the agglomeration of AgI nanoparticles to attain an excellent dispersibility [13]. Generally, Ag nanoparticles are inevitably generated in the photocatalytic reaction owing to the photo-induced decomposition of AgX [26,27]. For example, Chen et al. [28] observed that Ag was in-situ produced on $Ag_3PO_4$/AgI surface in photocatalytic degradation process, and the self-assembly $Ag_3PO_4$/Ag/AgI Z-scheme system improved the mobility of photogenerated carriers efficiently and increased the photostability. If Ag nanoparticles generated in AgI/$Bi_2WO_6$ heterojunction, it could transmit following the Z-scheme transfer model. Combining with those analysis, it is meaningful and desirable to construct a microspheres AgI/$Bi_2WO_6$ Z-scheme heterojunction to utilize the power of the sun for boosting photocatalytic performance.

Herein, a novel AgI/$Bi_2WO_6$ Z-scheme heterostructure was successfully constructed using an in situ precipitation way. The morphologies, composition, optical properties and electronic properties of the prepared photocatalysts were deeply analyzed. The photocatalytic properties of AgI/$Bi_2WO_6$ were tested for the degradation of refractory pollutant (tetracycline (TC), an antibiotic). The mineralization of TC with the photocatalyst was evaluated by total organic carbon (TOC), and further confirmed by three-dimensional excitation-emission matrix fluorescence spectra (3D EEMs). Ultimately, the Z-scheme charge transfer mechanism based on Ag nanoparticles as the electron mediator was proposed and affirmed by radicals trapping experiments and electron spin resonance (ESR) techniques.

## 2. Materials and methods

### 2.1. Materials

Bismuth nitrate pentahydrate ($Bi(NO_3)_3{\cdot}5H_2O$), sodium tungstate dihydrate ($Na_2WO_4{\cdot}2H_2O$), potassium iodide (KI), silver nitrate ($AgNO_3$), isopropyl alcohol (IPA), ethylenediamine tetra acetic acid disodium salt (EDTA-2Na), benzoquinone (BQ), and TC were all supplied by Chinese medicine group chemical reagent co., Ltd. Deionized water was adopted during the whole experiment.

### 2.2. Synthesis of $Bi_2WO_6$ microspheres and AgI/$Bi_2WO_6$ heterojunction

$Bi_2WO_6$ microspheres were synthesized through a facile hydrothermal procedure. Briefly, 1.94 g $Bi(NO_3)_3{\cdot}5H_2O$ was ultrasonically dissolved in 60 mL of 0.4 M nitric acid solution for 10 min. Then, 20 mL of 0.05 M $Na_2WO_4{\cdot}2H_2O$ solution was added slowly to the above suspension with vigorous stirring. After stirring 30 min, the resulting suspension was poured into a 100 mL Teflon-lined autoclave and heated to 160 °C for 20 h. The generated yellow powder was filtered, rinsed and vacuum dried at 60 °C for 8 h.

AgI/$Bi_2WO_6$ heterojunction was synthesized with a facile in-situ precipitation step. Firstly, 0.698 g of $Bi_2WO_6$ was ultrasonically dissolved into 50 mL deionized water for 5 min. Then, proportionate amounts $AgNO_3$ (0.156, 0.330, 0.743 and 1.982 mmol, respectively) was dissolved to the suspension above with magnetic stirring for 30 min under the dark condition. Next, 25 mL of KI (0.156, 0.330, 0.743 and 1.982 mmol, respectively) solution was dropwise added into the above suspension then stirred in the dark for 1 h. Finally, the sample was filtered, rinsed and vacuum dried at 60 °C for 12 h. The obtained products (AgI/$Bi_2WO_6$ = 0.05, 0.1, 0.2, 0.4) were defined as AgI (5 wt %)/$Bi_2WO_6$, AgI (10 wt%)/$Bi_2WO_6$, AgI (20 wt%)/$Bi_2WO_6$ and AgI (40 wt%)/$Bi_2WO_6$, respectively. Pure AgI was also synthesized using the identical method without adding $Bi_2WO_6$.

### 2.3. Characterization

The phase composition of the catalysts was measured by X-ray diffraction (XRD, Bruker, Germany). Scanning electron microscopy (SEM, S4800, Japan) was adopted for the morphology examination. Transmission electron microscopy (TEM, Tecnai G20) and high-resolution transmission electron microscopy (HRTEM, Tecnai G20) were used to investigate the microstructures. X-ray photoelectron spectroscopy (XPS) was selected to measure the valence state and surface elements of the samples. The specific surface area data was measured by Brunauer-Emmett-Teller (BET) based on a $N_2$ adsorption analyzer (Micromeritics ASAP 2460, USA). UV–vis diffuse reflectance spectra (DRS) were measured on a UV–vis spectrometer (Shimadzu, UV-2600). Shimazu TOC analyzer (TOC-VCPH) was provided to analysis the samples mineralization ability. 3D EEMs was provided by a F-4500 spectrofluorimeter. Photoluminescence (PL) spectra was performed on a spectrophotometer (Perkin Elmer, LS 55) under the excitation wavelength of 320 nm. Photocurrent (PC) responses were examined by an electrochemical workstation (CHI760E) in a three-electrode system. The electron spin resonance (ESR) measurements were verified by a Bruker ER200-SRC spectrometer ($\lambda > 420$ nm).

### 2.4. Photoreaction procedures

The visible photocatalytic performance of AgI/$Bi_2WO_6$ heterojunctions was evaluated by degradation of TC. In this experiment, a 300 W Xe lamp (CEL-HXF300) with a 420 nm cutoff filter was introduced as the light source. Before the experiment, 30 mg sample was thoroughly dispersed into TC solution (100 mL, 20 mg/L), followed by magnetically stirring in the dark for 30 min to achieve the absorption-desorption equilibrium of TC molecules on the surface of catalyst. Then, under visible light irradiation, 4 mL of mixed solution was collected with a syringe and filtered through a 0.45 μm organic filters. The concentration of TC molecules was analyzed by UV–vis spectroscopy with the certain absorption wavelength (357 nm for TC).

## 3. Results and discussion

### 3.1. Characterizations

The crystal structures of pure $Bi_2WO_6$, AgI, and AgI/$Bi_2WO_6$ heterojunctions were tested by XRD patterns. From Fig. 1, the peaks at 2$\theta$ values of 28.31°, 32.93°, 47.16°, and 55.83° could be observed, which matched well with the (113), (020), (220), and (313) planes of orthorhombic $Bi_2WO_6$ (JCPDS 73-1126) [29]. Besides, no any impurity phases were traced, indicating the prepared $Bi_2WO_6$ was unadulterated. The diffraction peaks of pure AgI at 2$\theta$ of 22.32°, 23.71°, 39.20°, and 46.31° were attributed to (100), (002), (110), and (112) crystal planes, respectively, as indexed by (JCPDS 09-0374) [2]. For the AgI/$Bi_2WO_6$ heterojunctions, the diffraction signals of $Bi_2WO_6$ and AgI were found

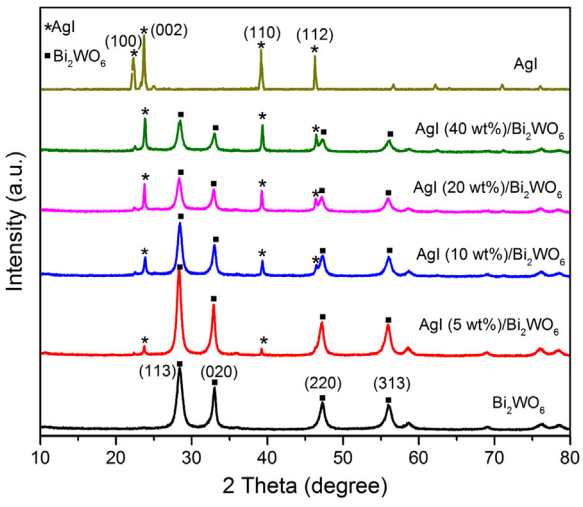


**Fig. 1.** XRD patterns of pure $Bi_2WO_6$, AgI, and AgI/$Bi_2WO_6$ heterojunctions.

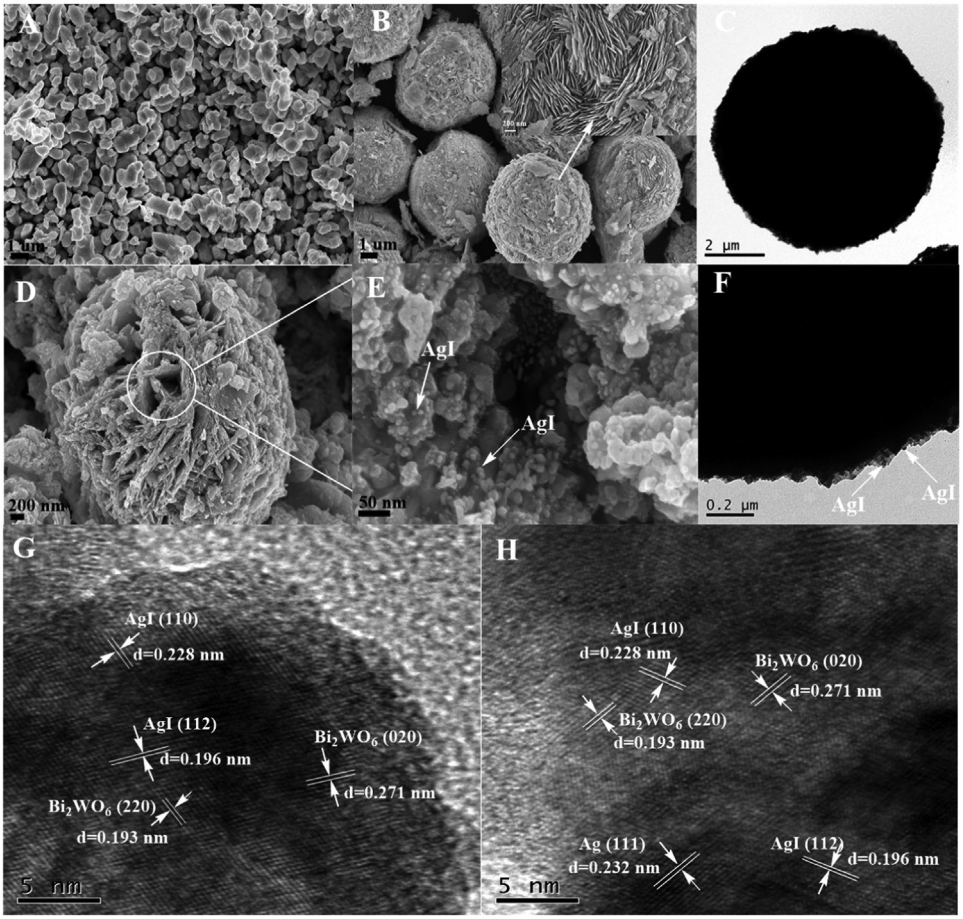


**Fig. 2.** SEM images of the as-prepared samples: (A) pure AgI, (B) pure $Bi_2WO_6$, and (D, E) AgI (20 wt%)/$Bi_2WO_6$; TEM images of pure $Bi_2WO_6$ (C), AgI (20 wt%)/$Bi_2WO_6$ (F), and HRTEM images of the fresh (G) and the used (H) AgI (20 wt%)/$Bi_2WO_6$.

obviously, while some peaks intensity of AgI were unconspicuous, which could be ascribed to the low amount and high dispersion of AgI nanoparticles in the heterojunctions [30].

The morphology of catalysts was characterized by SEM analysis. As depicted in Fig. 2A, pure AgI was composed of irregular nanoparticles with sizes of approximately 200–400 nm. Pure $Bi_2WO_6$ had a flower-like microspheres structure constructed by many 2D aligned nanosheets with a thickness of 10–20 nm (Fig. 2B). The SEM images of the AgI (20 wt%)/$Bi_2WO_6$ heterojunction were shown in Figs. 2D and 2E, the sample maintained hierarchical architectures to the $Bi_2WO_6$ flower-like microspheres. AgI nanoparticles were anchored on the $Bi_2WO_6$ nanosheet surface and had a smaller size than the pure AgI, which was probably the nanosheet acted as the clapboard to improve AgI dispersing, and decrease its grain size [31]. The microstructures of catalysts were further detected by TEM and HRTEM. As shown in Fig. 2C, the $Bi_2WO_6$ nanosheet combined with each other to form a sphere structure with diameters of 3.5–5 μm, which was consistent with SEM images. Since $Bi_2WO_6$ is sphere-like structure, AgI cannot be seen clearly and only some edge parts could be observed (Fig. 2F). In Fig. 2G, it was found that the lattice distances of 0.193 and 0.271 nm matched with the (220) and (020) crystal face of $Bi_2WO_6$. The lattice fringes with 0.196 and 0.228 nm accorded with the (112) and (110) plane of AgI. Moreover, the SEM image and its element mapping of AgI (20 wt%)/$Bi_2WO_6$ heterojunction were showed in Fig. S1. All the elements of Ag, I, Bi, W, and O could be observed in the heterojunctions. Based on the above results, it could be inferred that the AgI/$Bi_2WO_6$ heterojunctions have been successfully constructed.

XPS survey spectra was adopted to explore the element compositions and chemical valence states of AgI (20 wt%)/$Bi_2WO_6$ heterojunction. All signals of Ag, I, Bi, W, and O were observed in the XPS survey spectrum of AgI (20 wt%)/$Bi_2WO_6$ (Fig. 3A). Peaks located at 368 and 374.3 eV were attributed to Ag $3d_{5/2}$ and Ag $3d_{3/2}$ (Fig. 3B), which implied the presence of $Ag^+$ among AgI/$Bi_2WO_6$ composites and no $Ag^\circ$ was found [32]. XPS of I 3d could be separated to two peaks, locating at 619.5 and 630.9 eV, which could be referred to I $3d_{5/2}$ and I $3d_{3/2}$ of $I^-$ species (Fig. 3C) [33]. And the binding energies situated at 159.4 and 164.7 eV belonged to Bi $4f_{7/2}$ and Bi $4f_{5/2}$ orbits of $Bi^{3+}$ (Fig. 3D). Peaks at 35.6 and 37.8 eV corresponded to W $4f_{7/2}$ and W $4f_{5/2}$, showing the presence of $W^{6+}$ oxidized states (Fig. 3E). From Fig. 3F, the binding energies situated at 530.10 and 530.53 eV of O 1 s were assigned to the lattice oxygen of Bi-O and W-O bond in the form of $[WO_4]^{2-}$ and $[Bi_2O_2]^{2+}$ [34]. The XPS results provided irrefutable proof that heterostructure between AgI and $Bi_2WO_6$ were obtained.

Fig. 4 presented the nitrogen adsorption-desorption isotherms of $Bi_2WO_6$ and AgI (20 wt%)/$Bi_2WO_6$ heterojunction. Both of the samples had a type IV physisorption isotherms, demonstrating the existence of mesopores with the size of 2–50 nm. The specific surface area and pore characteristic of pure $Bi_2WO_6$ and AgI (20 wt%)/$Bi_2WO_6$ were summarized in Table 1. In comparison to pure $Bi_2WO_6$ (6.660 $m^2/g$), the surface area of AgI (20 wt%)/$Bi_2WO_6$ was higher (24.158 $m^2/g$). It was known that the material with larger specific surface area could offer abundant active sites and absorb more pollutants, thus leading to a higher photocatalytic activity.

### 3.2. Photocatalytic performance study

In Fig. 5A, the degradation of TC was negligible without catalyst, showing that TC was difficult to degrade directly by sunlight. Only

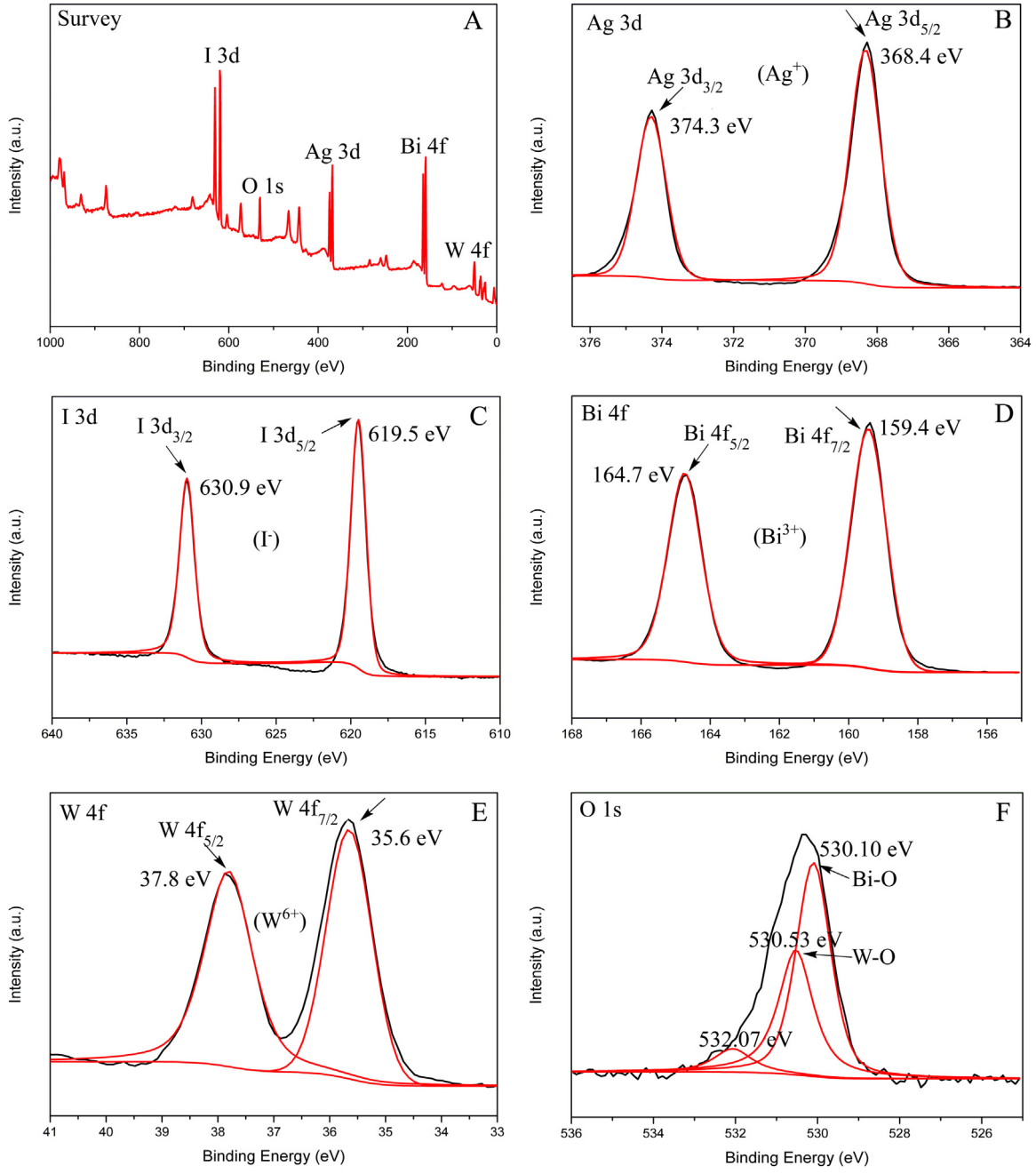


**Fig. 3.** XPS spectra of AgI (20 wt%)/$Bi_2WO_6$ heterojunction: (A) survey, (B) Ag 3d, (C) I 3d, (D) Bi 4f, (E) W 4f, and (F) O 1s.

about 60.75% degradation appeared when pure $Bi_2WO_6$ exists, while 73.37% degradation occurred with pure AgI after 60 min irradiation. Compared to pure $Bi_2WO_6$ and AgI, the AgI/$Bi_2WO_6$ heterojunction exhibited superior photocatalytic performance. The optimal catalyst with 20 wt% AgI modification showed the highest degradation efficiency, about 93.05% of TC was removed within 60 min irradiation. With the amount of AgI exceeded 20 wt%, the photocatalytic activity of the AgI/$Bi_2WO_6$ heterojunctions then decreased. It was probably due to the excessive AgI nanoparticles blocked the irradiation to the surface of $Bi_2WO_6$, leading to the decrease of the generation of photogenerated carriers [35,36]. However, too little AgI doping decreased the light absorption intensity. Based on the results of absorption ability tests (Fig. S2), the adsorption-desorption equilibrium of pollutants and catalysts was attained within 30 min dark treatment. The adsorption ratio of $Bi_2WO_6$ was greatly improved when AgI (20 wt%) nanoparticles anchored on its surface, which was identical with the result of the nitrogen adsorption test.

The photodegradation of TC process was fitted well with a pseudo-first-order kinetic model: -ln ($C_t$ /$C_0$) = $kt$, where $k$ represent the rate constant ($min^{-1}$), $C_0$ and $C_t$ represent the TC concentrations at irradiation time 0 and t, respectively. From Fig. 5B, AgI (20 wt%)/$Bi_2WO_6$ displayed the maximum rate constant of 0.075 $min^{-1}$, which reached 5.4 and 3.3 times higher than pure $Bi_2WO_6$ (0.014 $min^{-1}$) and AgI (0.023 $min^{-1}$) nanoparticles. The reaction rate constant ($k$) values, correlation coefficients ($R^2$) and the efficiency of photocatalytic degradation of the prepared sample towards TC were summarized in Table S1. The results showed that the photocatalytic performance of $Bi_2WO_6$ was significantly improved due to the formation of AgI/$Bi_2WO_6$ heterojunction.

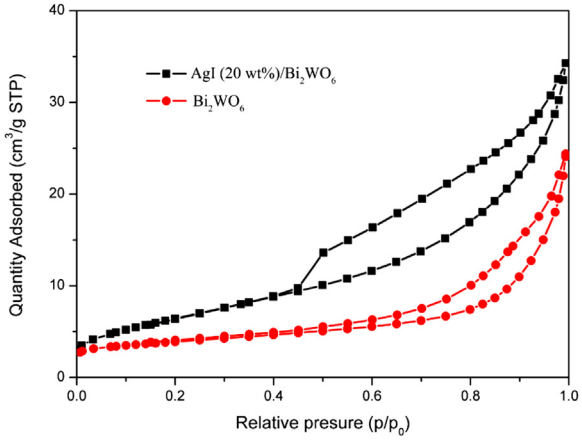


**Fig. 4.** Nitrogen adsorption-desorption isotherm of pure $Bi_2WO_6$ and AgI (20 wt %)/$Bi_2WO_6$ heterojunction.

**Table 1**
Surface area, pore size and pore volume parameters for pure $Bi_2WO_6$ and AgI (20 wt%)/$Bi_2WO_6$ heterojunction.

| Samples | Surface area[a] ($m^2$/g) | Pore size[b] (nm) | $V_t$[c] ($cm^3$/g) |
|---|---|---|---|
| $Bi_2WO_6$ | 6.660 | 17.431 | 0.020 |
| AgI (20 wt%)/$Bi_2WO_6$ | 24.158 | 18.254 | 0.040 |

[a] Measured using $N_2$ adsorption with the Brunauer-Emmett-Teller (BET) method.
[b] Pore size in diameter calculated by the desorption data using Barrett-Joyner-Halenda (BJH) method.
[c] Total pore volume determined at $P/P_0 = 0.95$.

### 3.3. Mineralization ability of AgI/$Bi_2WO_6$ for TC and 3D EEMs analysis

The mineralization ability of photocatalysts is also a basic parameter for evaluating photocatalytic activity. Fig. S3 presented the degradation efficiency of TC based on TOC removal by the AgI (20 wt %)/$Bi_2WO_6$ heterojunction. About 42.28% of TOC was removed after 60 min reaction, and almost 74.25% removal was obtained after 180 min, indicating that the TC mineralization by the AgI (20 wt %)/$Bi_2WO_6$ heterojunction is possible. To further explore the mineralization and degradation properties of photocatalysts, 3D EEMs (excitation-emission matrix fluorescence spectroscopy) analysis was adopted. As revealed in Fig. 6A, no fluorescence signals were found towards the initial TC solution. After 30 min irradiation (Fig. 6B), two fluorescence peaks at $E_x/E_m$ = 240–260/350–380 nm and $E_x/E_m$ = 285–325/380–430 nm appeared. Based on the Chen's reports [37], the two peaks referring to the aromatic hydrocarbons and humic acids-like substance, respectively. This phenomenon indicated that the molecular structure of TC has been partly destroyed or intermediates were generated in the process of photodegradation. With the irradiation time extended to 180 min (Fig. 6D), the intensity of the aromatic hydrocarbons peaks weakened and the intensity of the humic acids-like substance peaks enhanced, suggesting that TC molecules could be further degraded. The above results showed that AgI (20 wt%)/$Bi_2WO_6$ displayed excellent mineralization ability.

### 3.4. Photocatalyst stability tests

The photostability of the catalyst plays an important role for practical applications. From Fig. S4, the degradation efficiency of TC after cycle experiment was determined to be about 93.05%, 92.41%, 90.50%, and 89.24% for 1st, 2nd, 3rd, and 4th run, respectively. The photocatalytic efficiency decreased by only 3.81% after four run, indicating the good photostability of the AgI (20 wt%)/$Bi_2WO_6$ heterojunction. Furthermore, the cycled AgI (20 wt%)/$Bi_2WO_6$ heterojunction was tested by HRTEM, XRD, and XPS. As revealed in Fig. 7A and B, there was a slightly different before and after reaction. The diffraction peak situated at 38.38° was observed in the used material which represented the (111) crystal face of metallic Ag (JCPDS 65-2871) [22], indicating the producing of the Ag nanoparticles during the irradiation. Meanwhile, the HRTEM picture of the used AgI (20 wt%)/$Bi_2WO_6$ was depicted in Fig. 2H. The *d*-spacing at 0.232 nm referred to (111) lattice plane of Ag (JCPDS 65-2871). To further prove the production of Ag nanoparticles, the XPS peak of the used AgI (20 wt%)/$Bi_2WO_6$ was resolved into four peaks (Fig. 7C). Peaks with binding energy of 368.1, 368.3, 374.1 and 374.5 eV were assigned to $Ag^+$ $3d_{5/2}$, $Ag^0$ $3d_{5/2}$, $Ag^+$ $3d_{3/2}$ and $Ag^0$ $3d_{3/2}$ [38], respectively. In Fig. 7D, the molar ratio of Ag/I in the used AgI (20 wt%)/$Bi_2WO_6$ was higher than the theory results (1:1) for the fresh AgI (20 wt%)/$Bi_2WO_6$ and evaluated to be 1.07:1. Synthesizing all the above proofs, the existence of metallic Ag was demonstrated, and it could accelerate the separation and transfer of photogenerated electrons and holes, displaying the improved photocatalytic performance.

### 3.5. Light absorption and charge transfer properties

UV–vis diffuse reflectance spectra (DRS) were adopted to analyze the visible light absorption capacity and optical bandgap of the samples. As presented in Fig. 8A, the absorption edge was observed to be about 450 nm for $Bi_2WO_6$ and 480 nm for AgI. Obviously, the AgI

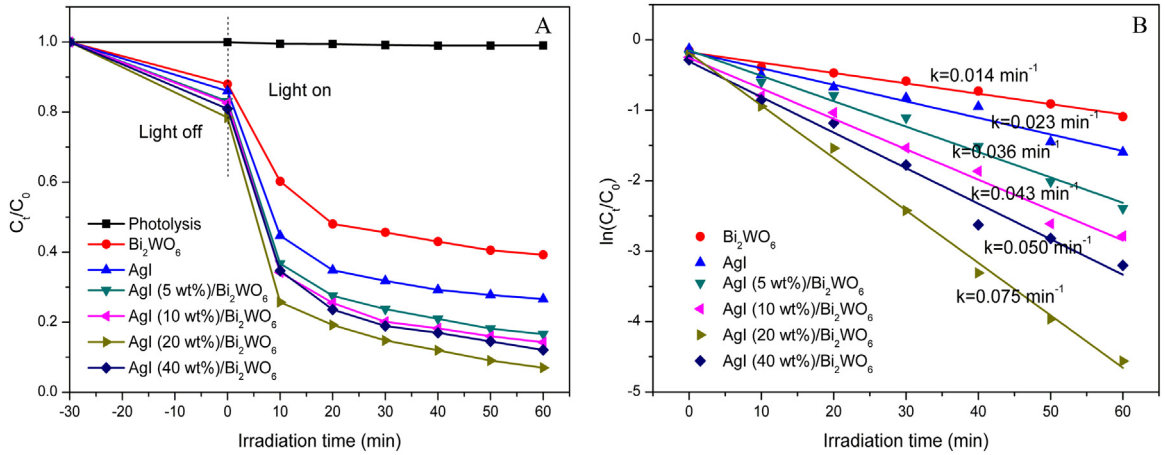


**Fig. 5.** (A) Photodegradation of TC by using pure $Bi_2WO_6$, AgI, and AgI/$Bi_2WO_6$ heterojunctions under visible light irradiation; (B) the pseudo-first-order kinetics of TC degradation.

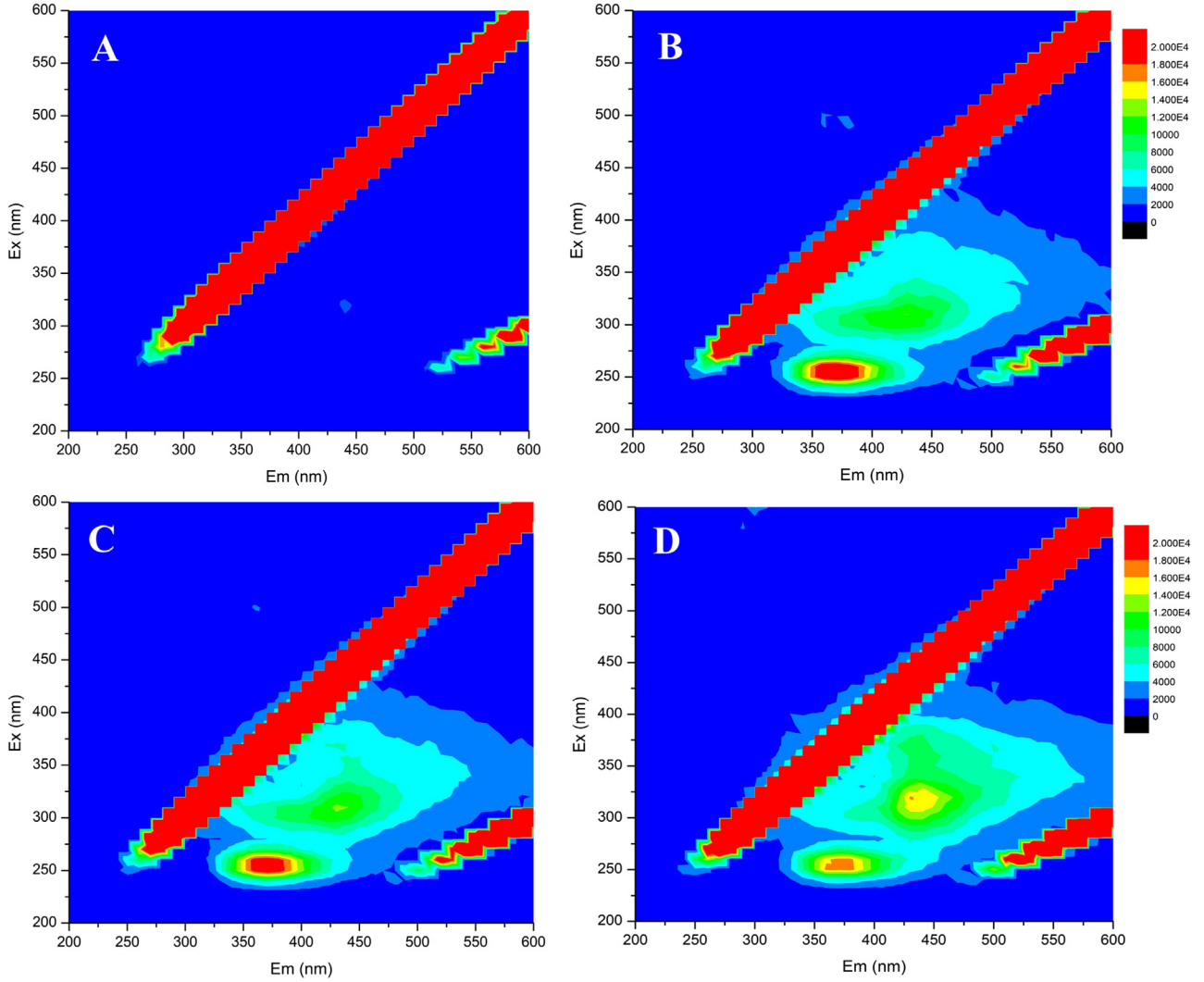


**Fig. 6.** 3D EEMs of the TC aqueous solution: (A) taken from the original solution; (B-D) obtained after an irradiation time of 30, 60, and 180 min, respectively.

(20 wt%)/$Bi_2WO_6$ heterojunction possessed a wider absorption in visible area, indicating that more visible light could be utilized to produce photogenerated carriers. In general, the absorption band-gap ($E_g$) of $Bi_2WO_6$ and AgI could be obtained according to Kubelka-Munk equation [39].

$$ahv = A(hv - E_g)^{n/2} \quad (1)$$

where $\alpha$, $h$, $v$, $A$ and $E_g$ represent the absorption coefficient, planck constant, light frequency, a constant and band gap energy, respectively. The value of n for $Bi_2WO_6$ and AgI was both estimated to be 1 because of a direct optical transition type [40,41]. Thus, as displayed in Fig. 8B, the band gaps for the $Bi_2WO_6$ and AgI were approximately 2.70 eV and 2.74 eV, respectively. Furthermore, the conduction band edge ($E_{CB}$) and value band edge ($E_{VB}$) of a semiconductor could be achieved through the formulas below [32]:

$$E_{CB} = X - E^e - 0.5E_g \quad (2)$$

$$E_{VB} = E_{CB} + E_g \quad (3)$$

where $X$ refers to the electronegativity of the semiconductor, $E^e$ is the energy of free electrons on the hydrogen scale (about 4.5 eV) [2], and $E_g$ represent the energy gap of semiconductors. The $X$ values for $Bi_2WO_6$ and AgI are 6.36 and 5.49 eV, respectively. Based on the above equations, the $E_{CB}$ values of $Bi_2WO_6$ and AgI were estimated to be 0.51 and −0.38 eV, with the homologous $E_{VB}$ values of $Bi_2WO_6$ and AgI being 3.21 and 2.36 eV.

PL spectra were adopted to study the migration and recombination process of photogenerated charges over semiconductors [42]. The PL spectra of the pure $Bi_2WO_6$ and modified $Bi_2WO_6$ were depicted in Fig. 8C. It was found that the emission peak of $Bi_2WO_6$ microspheres was increased after decoration of AgI. The PL intensity of the AgI (20 wt %)/$Bi_2WO_6$ heterojunction exhibited the strongest emission, indicating that the recombination rate of photogenerated electrons and holes on the surface of AgI (20 wt%)/$Bi_2WO_6$ heterojunction was the highest. The PL spectra results appears to contradict with the traditional heterojunctions which typically exhibit weakened PL intensity [2,7,39]. The higher PL intensity of AgI (20 wt%)/$Bi_2WO_6$ could be interpreted by the recombination of photogenerated electrons at the CB of $Bi_2WO_6$ and the hole at the VB of AgI, which actually enhance the photocatalytic activity of catalysts with Z-scheme heterojunctions [43].

Generally, the higher photocurrent intensity indicates more efficient separation of photogenerated electron-hole pairs [39]. In order to further explore the electron transfer process, the PC response of pure $Bi_2WO_6$, AgI, and AgI (20 wt%)/$Bi_2WO_6$ heterojunction was measured (Fig. 8D). Obviously, the photocurrent intensity of AgI (20 wt %)/$Bi_2WO_6$ was higher than pure $Bi_2WO_6$ and AgI, which was almost 2.5 folds than pure AgI, showing the higher separation efficiency of photogenerated electron-hole pairs in AgI/$Bi_2WO_6$ heterojunction. According to the results of PC, it could further confirm that the AgI modified $Bi_2WO_6$ could effectively improve the separation and transfer

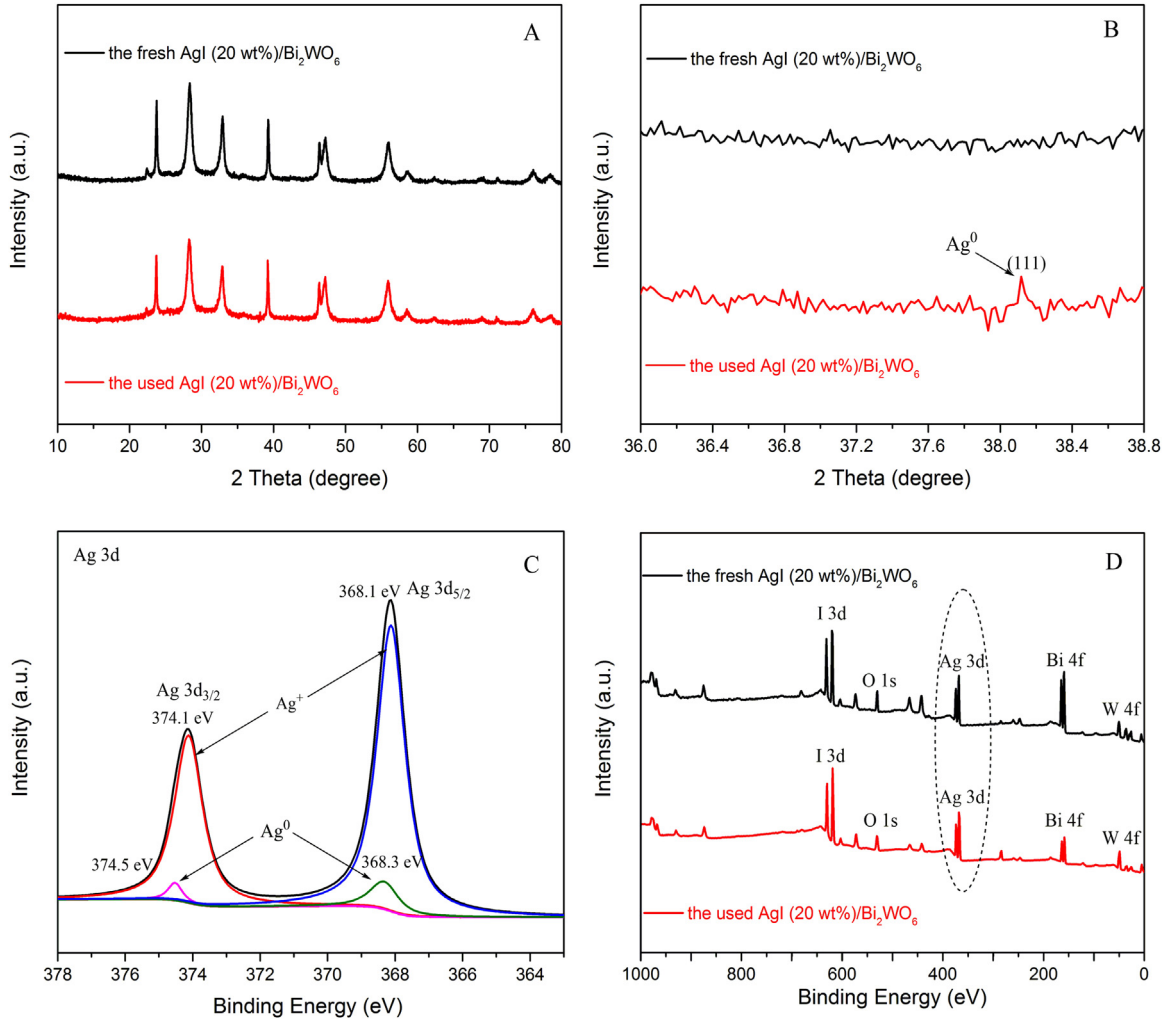


**Fig. 7.** (A, B) XRD patterns of AgI (20 wt%)/$Bi_2WO_6$ before and after photocatalytic tests; (C) Ag 3d XPS spectra of the AgI (20 wt%)/$Bi_2WO_6$ after photoreaction; (D) the survey XPS spectra of AgI (20 wt%)/$Bi_2WO_6$ before and after photocatalytic tests.

of photogenerated carriers.

### 3.6. Photocatalytic mechanism study

Three quenchers, benzoquinone (BQ, $\cdot O_2^-$ scavenger), ethylenediaminetetraacetic acid disodium (EDTA-2Na, $h^+$ scavengers), and isopropanol (IPA, •OH scavenger), were added to the solution before photodegradation of TC. From Fig. 9A, it was observed that the addition of BQ, EDTA-2Na, or IPA presented negative impact on AgI (20 wt %)/$Bi_2WO_6$ photocatalytic performance. The degradation efficiency of TC decreased from 93.05% to 47.08% (BQ), 38.48% (EDTA-2Na), and 62.45% (IPA) within 60 min, respectively (Fig. 9B). Thus, it could be inferred that $\cdot O_2^-$, $h^+$ and •OH radical took effect jointly in the degradation procedure. In order to further prove the radical species generation in the photodegradation reaction, the ESR measurements were adopted. Fig. 9C and D presented the DMPO spin-trapping ESR spectra of AgI (20 wt%)/$Bi_2WO_6$. As indicated in Fig. 9C and D, neither DMPO-$\cdot O_2^-$ nor DMPO-•OH signals were detected in dark condition. After exposed to the visible light, the signals of DMPO-$\cdot O_2^-$ and DMPO-•OH could be detected obviously. The results indicated that both $\cdot O_2^-$ and •OH radicals were generated during the photocatalytic reaction. Hence, the radical species trapping and ESR analysis revealed the significant role of $\cdot O_2^-$, $h^+$ and •OH, resulting the enhancement of the photocatalytic activity towards TC degradation.

According to the above results, the following three factors account for the desirable photocatalytic activity of the catalyst: the high specific surface area, enhanced visible light absorption capacity, and efficient charge separation. In addition, it had been proved that the Ag nanoparticles were generated based on the result of XRD, XPS, and HRTEM analysis, which could act as a charge transmission bridge to reduce the distance of electron transfer between the semiconductors and accelerating the separation of photogenerated charge carriers. According to the above analysis, a synergistic mechanism for the TC degradation by AgI (20 wt%)/$Bi_2WO_6$ heterojunction was proposed in Fig. 10. As presented in Fig. 10A, photogenerated electrons on the CB of AgI would migrate to Ag nanoparticles and were then transferred to the CB of $Bi_2WO_6$, and the photogenerated holes on the VB of $Bi_2WO_6$ would migrate to the VB of AgI, leading to the rapid separation of the electrons and holes. However due to the CB potential (0.51 eV) of the $Bi_2WO_6$ was more positive than the $O_2/\cdot O_2^-$ potential (-0.33 eV vs. NHE) [44], the electrons generated in the CB of $Bi_2WO_6$ had no power to reduce $O_2$ into $\cdot O_2^-$. Moreover, the accumulated $h^+$ in the VB of AgI could not oxidize $OH^-$ to form •OH because the VB potential (2.36 eV) of the AgI was less positive than the $\cdot OH/OH^-$ potential (2.40 eV vs. NHE) [38]. Therefore, only the holes played a part in the reaction system, which was inconsistent with the radical trapping and ESR analysis. It might be unreasonable to conclude the photogenerated electrons and holes in AgI (20 wt%)/$Bi_2WO_6$ heterojunction transfer by the traditional heterojunction system. The Z-scheme transfer system could be more suitable (Fig. 10B). The electrons formed on the CB of $Bi_2WO_6$ would shift to

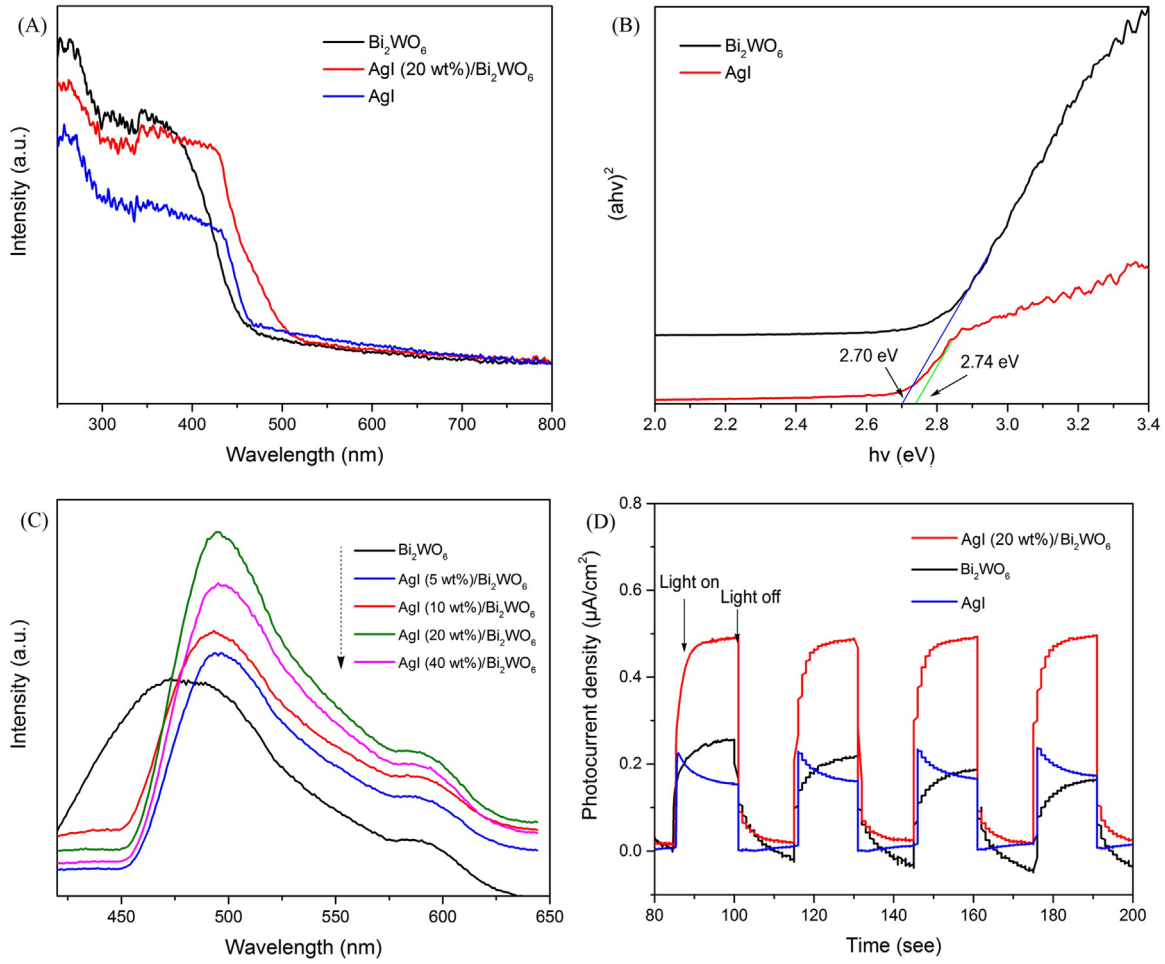


**Fig. 8.** (A) UV–vis diffuse reflectance spectra of pure $Bi_2WO_6$, AgI, and AgI (20 wt%)/$Bi_2WO_6$; (B) The optical bandgap of pure $Bi_2WO_6$ and AgI; (C) PL spectra of the pure $Bi_2WO_6$ and modified $Bi_2WO_6$; (D) PC responses of pure $Bi_2WO_6$, AgI, and AgI (20 wt%)/$Bi_2WO_6$.

metallic Ag, and then recombined with the holes that transferred from the VB of AgI, thus, leading to the rapid separation of electron-hole pairs. Meanwhile, the photogenerated electrons in the CB of AgI could reduce the adsorbed $O_2$ into $\bullet O_2^-$ because the CB potential of AgI was more negative than the $O_2/\bullet O_2^-$ potential (-0.33 eV vs. NHE). In addition, the $O_2$ adsorbed on the surface of AgI could also combine with $H_2O$ molecules and electrons to produce $H_2O_2$, which could be further generated to •OH. The holes accumulated in the VB of $Bi_2WO_6$ could react with $OH^-$ to generate •OH or oxidize organic pollutants directly, which attributed to the potential of VB of $Bi_2WO_6$ was more positive than the $\bullet OH/OH^-$ potential (2.40 eV vs. NHE). This result was accorded with the finding of the radical trapping and ESR analysis. In summary, the Z-scheme system significantly accelerated the separation of photogenerated electrons and holes, leading to the superior photocatalytic performance. Finally, the photocatalytic reaction mainly includes the following:

$$AgI/Bi_2WO_6 + hv \rightarrow AgI/Bi_2WO_6(e^- + h^+) \quad (4)$$

$$e^- + O_2 \rightarrow \cdot O_2^- \quad (5)$$

$$\cdot O_2^- + 2H^+ + e^- \rightarrow H_2O_2 \quad (6)$$

$$H_2O_2 + e^- \rightarrow \cdot OH + OH^- \quad (7)$$

$$(\cdot O_2^-, h^+ \text{and} \cdot OH) + TC \rightarrow \text{degraded or mineralized products} \quad (8)$$

## 4. Conclusions

All in all, the novel AgI/$Bi_2WO_6$ heterojunctions were successfully synthesized via an in situ precipitation method. Under visible light irradiation, the AgI (20 wt%)/$Bi_2WO_6$ heterojunction displayed the best photocatalytic activity with 93.05% removal of TC within 60 min. Meanwhile, 74.25% of TOC removal was obtained within 180 min, showing that the AgI/$Bi_2WO_6$ heterojunction displayed the excellent mineralization ability to degrade TC which was further proved by 3D EEMs. The improved photocatalytic activity of AgI/$Bi_2WO_6$ mainly originated from the synergistic effects including high specific surface area, enhanced visible light absorption capacity, and the efficient separation and transfer of photogenerated carriers based on a Z-scheme system that consisted of $Bi_2WO_6$, AgI, and Ag. Accordingly, radical trapping experiments and ESR techniques demonstrated the significant role $\bullet O_2^-$, $h^+$ and •OH played in the photodegradation process. Moreover, the degradation efficiency of TC was no visible decline after four consecutive processes under the same condition (only 3.81% loss), showing the good photostability of AgI/$Bi_2WO_6$. This work provides a new insight to design and construct a Z-scheme heterojunction photocatalyst for environmental remediation and energy utilization.

## Acknowledgements

This work was financially supported by the Program for the National Natural Science Foundation of China (51879101, 51579098, 51779090, 51709101, 51521006, 51809090, 51278176, 51378190),

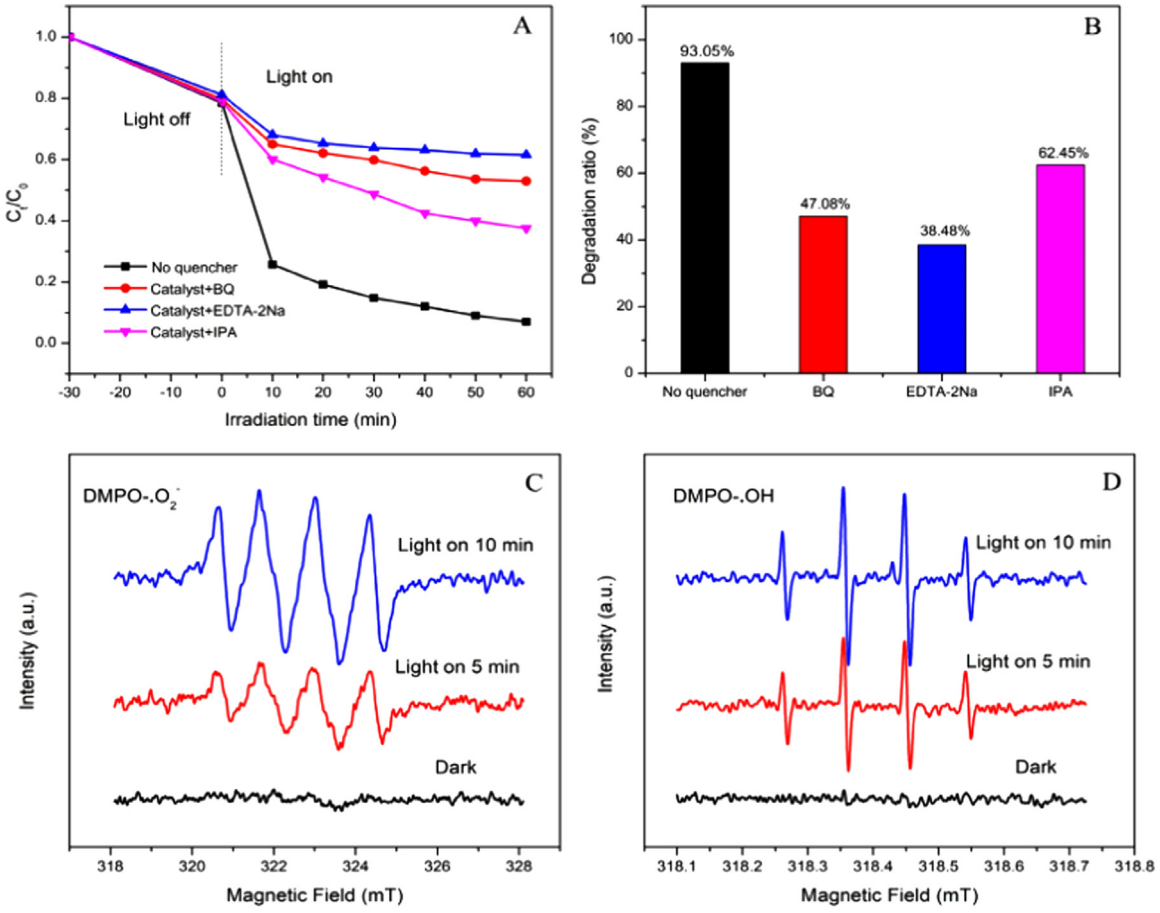


**Fig. 9.** (A) Photocatalytic curves of AgI (20 wt%)/$Bi_2WO_6$ heterojunction with different scavengers for the degradation of TC; (B) Photodegradation efficiency of TC over AgI (20 wt%)/$Bi_2WO_6$ by addition of 2 mM BQ, 10 mM EDTA-2Na, and 10 mM IPA; (C) DMPO spin-trapping ESR spectra for AgI (20 wt%)/$Bi_2WO_6$ in methanol dispersion for DMPO- •$O_2^-$; (D) in aqueous dispersion for DMPO- •OH.

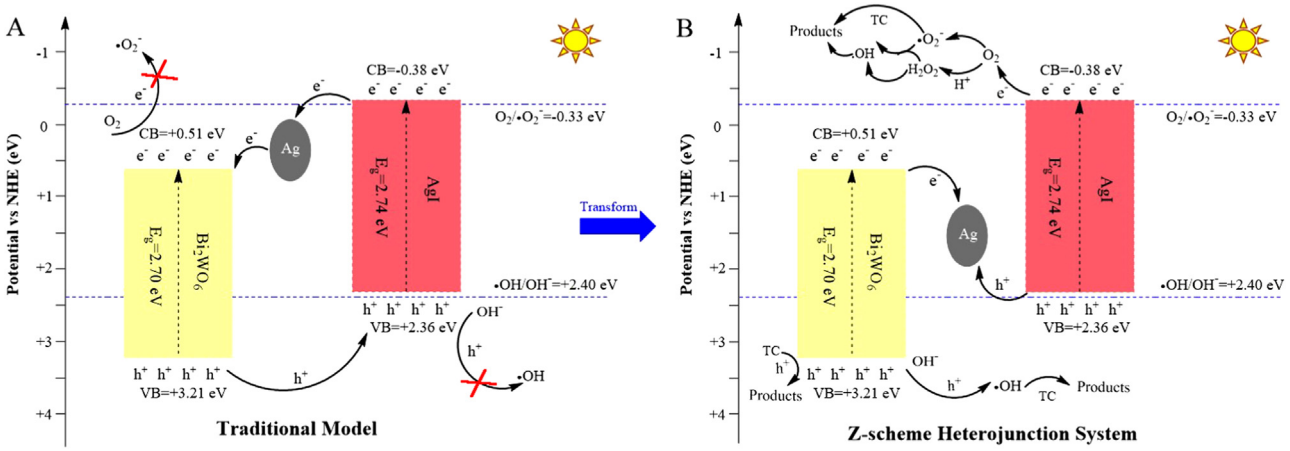


**Fig. 10.** Schematic illustration of the mechanism for the photocatalytic degradation of TC under visible light irradiation over AgI/$Bi_2WO_6$ heterojunction: (A) Traditional model and (B) Z-scheme heterojunction system.

the National Program for Support of Top-Notch Young Professionals of China (2014), the Program for Changjiang Scholars and Innovative Research Team in University (IRT-13R17), and Hunan Provincial Science and Technology Plan Project (2018SK20410, 2017SK2243, 2016RS3026), and the Fundamental Research Funds for the Central Universities (531109200027, 531107051080, 531107050978).

## Appendix A. Supporting information

Supplementary data associated with this article can be found in the online version at doi:10.1016/j.ceramint.2018.12.119.

## References

[1] R. Asahi, T. Morikawa, T. Ohwaki, K. Aoki, Y. Taga, Visible-light photocatalysis in nitrogen-doped titanium oxides, Science 293 (2001) 269–271.

[2] X.J. Wen, C.G. Niu, M. Ruan, L. Zhang, G.M. Zeng, AgI nanoparticles-decorated $CeO_2$ microsheets photocatalyst for the degradation of organic dye and tetracycline under visible-light irradiation, J. Colloid Interface Sci. 497 (2017) 368–377.

[3] C. Hu, D. Huang, G. Zeng, M. Cheng, X. Gong, R. Wang, W. Xue, Z. Hu, Y. Liu, The combination of Fenton process and Phanerochaete chrysosporium for the removal of bisphenol A in river sediments: mechanism related to extracellular enzyme, organic acid and iron, Chem. Eng. J. 338 (2018) 432–439.

[4] Q. Zhang, Z. Dai, G. Cheng, Y.L. Liu, R. Chen, In-situ room-temperature synthesis of amorphous/crystalline contact $Bi_2S_3/Bi_2WO_6$ heterostructures for improved photocatalytic ability, Ceram. Int. 43 (2017) 11296–11304.

[5] H. Wang, L. Zhang, Z. Chen, J. Hu, S. Li, Z. Wang, J. Liu, X. Wang, Semiconductor heterojunction photocatalysts: design, construction, and photocatalytic performances, Chem. Soc. Rev. 43 (2014) 5234–5244.

[6] S. Morelli, R. Pérez, A. Querejeta, J. Muñoz, L. Lusvarghi, M.L. Gualtieri, G. Bolelli, H.J. Grande, Photocatalytic enamel/$TiO_2$ coatings developed by electrophoretic deposition for methyl orange decomposition, Ceram. Int. 44 (2018) 16199–16208.

[7] S. Banerjee, S.C. Pillai, P. Falaras, K.E. O'shea, J.A. Byrne, D.D. Dionysiou, New insights into the mechanism of visible light photocatalysis, J. Phys. Chem. Lett. 5 (2014) 2543–2554.

[8] Z. Wang, T. Hu, K. Dai, J. Zhang, C. Liang, Construction of Z-scheme $Ag_3PO_4$/$Bi_2WO_6$ composite with excellent visible-light photodegradation activity for removal of organic contaminants, Chin. J. Catal. 38 (2017) 2021–2029.

[9] X. Meng, Z. Li, H. Zeng, J. Chen, Z. Zhang, $MoS_2$ quantum dots-interspersed $Bi_2WO_6$ heterostructures for visible light-induced detoxification and disinfection, Appl. Catal., B 210 (2017) 160–172.

[10] K. Kadeer, Y. Tursun, T. Dilinuer, K. Okitsu, A. Abulizi, Sonochemical preparation and photocatalytic properties of CdS QDs/$Bi_2WO_6$ 3D heterojunction, Ceram. Int. 44 (2018) 13797–13805.

[11] Y. Liu, L. Chen, Q. Yuan, J. He, C.T. Au, S.F. Yin, A green and efficient photocatalytic route for the highly-selective oxidation of saturated alpha-carbon C-H bonds in aromatic alkanes over flower-like $Bi_2WO_6$, Chem. Commun. 52 (2016) 1274–1277.

[12] D. Huang, X. Wang, C. Zhang, G. Zeng, Z. Peng, J. Zhou, M. Cheng, R. Wang, Z. Hu, X. Qin, Sorptive removal of ionizable antibiotic sulfamethazine from aqueous solution by graphene oxide-coated biochar nanocomposites: influencing factors and mechanism, Chemosphere 186 (2017) 414–421.

[13] L. Zhang, Y. Zhu, A review of controllable synthesis and enhancement of performances of bismuth tungstate visible-light-driven photocatalysts, Catal. Sci. Technol. 2 (2012) 694–706.

[14] G. Long, J. Ding, L. Xie, R. Sun, M. Chen, Y. Zhou, X. Huang, G. Han, Y. Li, W. Zhao, Fabrication of mediator-free g-$C_3N_4/Bi_2WO_6$ Z-scheme with enhanced photocatalytic reduction dechlorination performance of 2,4-DCP, Appl. Surf. Sci. 455 (2018) 1010–1018.

[15] C. Li, G. Chen, J. Sun, J. Rao, Z. Han, Y. Hu, W. Xing, C. Zhang, Doping effect of phosphate in $Bi_2WO_6$ and universal improved photocatalytic activity for removing various pollutants in water, Appl. Catal., B 188 (2016) 39–47.

[16] J.X. Low, J.G. Yu, M. Jaroniec, S. Wageh, A.A. Al-Ghamdi, Heterojunction photocatalysts, Adv. Mater. 29 (2017) 1601694.

[17] S. Issarapanacheewin, K. Wetchakun, S. Phanichphant, W. Kangwansupamonkon, N. Wetchakun, Efficient photocatalytic degradation of Rhodamine B by a novel $CeO_2/Bi_2WO_6$ composite film, Catal. Today 278 (2016) 280–290.

[18] H. Wang, J. Lu, F. Wang, W. Wei, Y. Chang, S. Dong, Preparation, characterization and photocatalytic performance of g-$C_3N_4/Bi_2WO_6$ composites for methyl orange degradation, Ceram. Int. 40 (2014) 9077–9086.

[19] J. Tian, Y. Sang, G. Yu, H. Jiang, X. Mu, H. Liu, A $Bi_2WO_6$–based hybrid photocatalyst with broad spectrum photocatalytic properties under UV, visible, and near-infrared irradiation, Adv. Mater. 25 (2013) 5075–5080.

[20] D. Huang, X. Yan, M. Yan, G. Zeng, C. Zhou, J. Wan, M. Cheng, W. Xue, Graphitic carbon nitride-based heterojunction photoactive nanocomposites: applications and mechanism insight, ACS Appl. Mater. Interfaces 10 (2018) 21035–21055.

[21] X. Liu, Q. Lu, J. Liu, Electrospinning preparation of one-dimensional ZnO/$Bi_2WO_6$ heterostructured sub-microbelts with excellent photocatalytic performance, J. Alloy. Compd. 662 (2016) 598–606.

[22] H. Yu, L. Xu, P. Wang, X. Wang, J. Yu, Enhanced photoinduced stability and photocatalytic activity of AgBr photocatalyst by surface modification of Fe (III) cocatalyst, Appl. Catal., B 144 (2014) 75–82.

[23] H. Zhang, X. Fan, X. Quan, S. Chen, H. Yu, Graphene sheets grafted Ag@AgCl hybrid with enhanced plasmonic photocatalytic activity under visible light, Environ. Sci. Technol. 45 (2011) 5731–5736.

[24] S. Zhang, Z. Liu, Y. Zhang, S. Gao, R. Jin, Q. Wang, Highly effective photoelectrochemical performance of solar energy materials based on $Ag_2WO_4$-AgX (X = Cl, Br, I) sensitized $TiO_2$ nanotube arrays, Ceram. Int. 44 (2018) 6659–6665.

[25] Q. Wang, X. Shi, J. Xu, J.C. Crittenden, E. Liu, Y. Zhang, Y. Cong, Highly enhanced photocatalytic reduction of Cr (VI) on AgI/$TiO_2$ under visible light irradiation: influence of calcination temperature, J. Hazard. Mater. 307 (2016) 213–220.

[26] L. Ye, J. Liu, C. Gong, L. Tian, T. Peng, L. Zan, Two different roles of metallic Ag on Ag/AgX/BiOX (X = Cl, Br) visible light photocatalysts: surface plasmon resonance and Z-scheme bridge, ACS Catal. 2 (2012) 1677–1683.

[27] D. Huang, R. Wang, Y. Liu, G. Zeng, C. Lai, P. Xu, B.A. Lu, J.J. Xu, C. Wang, C. Huang, Application of molecularly imprinted polymers in wastewater treatment: a review, Environ. Sci. Pollut. R. 22 (2015) 963–977.

[28] Z. Chen, W. Wang, Z. Zhang, X. Fang, High-efficiency visible-light-driven $Ag_3PO_4$/AgI photocatalysts: z-scheme photocatalytic mechanism for their enhanced photocatalytic activity, J. Phys. Chem. C. 117 (2013) 19346–19352.

[29] Y. Su, G. Tan, T. Liu, L. Lv, Y. Wang, X. Zhang, Z. Yue, H. Ren, A. Xia, Photocatalytic properties of $Bi_2WO_6/BiPO_4$ Z-scheme photocatalysts induced by double internal electric fields, Appl. Surf. Sci. 457 (2018) 104–114.

[30] X.J. Wen, C.G. Niu, L. Zhang, G.M. Zeng, Novel p-n heterojunction BiOI/$CeO_2$ photocatalyst for wider spectrum visible-light photocatalytic degradation of refractory pollutants, Dalton Trans. 46 (2017) 486–493.

[31] F. Li, B. Dong, Construction of novel Z-scheme $Cu_2O$/graphene/α-$Fe_2O_3$ nanotube arrays composite for enhanced photocatalytic activity, Ceram. Int. 43 (2017) 16007–16012.

[32] L. Kong, Z. Jiang, H.H. Lai, R.J. Nicholls, T. Xiao, M.O. Jones, P.P. Edwards, Unusual reactivity of visible-light-responsive AgB-BiOBr heterojunction photocatalysts, J. Catal. 293 (2012) 116–125.

[33] H. Zhang, C.G. Niu, X.J. Wen, Y. Wang, G.M. Zeng, Enhanced visible light photocatalytic activity of $CdMoO_4$ microspheres modified with AgI nanoparticles, Catal. Commun. 86 (2016) 124–128.

[34] L. Yue, S. Wang, G. Shan, W. Wu, L. Qiang, L. Zhu, Novel MWNTs–$Bi_2WO_6$ composites with enhanced simulated solar photoactivity toward adsorbed and free tetracycline in water, Appl. Catal., B 176 (2015) 11–19.

[35] X.J. Wen, C.G. Niu, D.W. Huang, L. Zhang, C. Liang, G.M. Zeng, Study of the photocatalytic degradation pathway of norfloxacin and mineralization activity using a novel ternary Ag/AgCl-$CeO_2$ photocatalyst, J. Catal. 355 (2017) 73–86.

[36] W. Xue, D. Huang, G. Zeng, J. Wan, C. Zhang, R. Xu, M. Cheng, R. Deng, Nanoscale zero-valent iron coated with rhamnolipid as an effective stabilizer for immobilization of Cd and Pb in river sediments, J. Hazard. Mater. 341 (2018) 381–389.

[37] W. Chen, P. Westerhoff, J.A. Leenheer, K. Booksh, Fluorescence excitation- emission matrix regional integration to quantify spectra for dissolved organic matter, Environ. Sci. Technol 37 (2003), pp. 5701–5710.

[38] X.J. Wen, C.G. Niu, L. Zhang, C. Liang, H. Guo, G.M. Zeng, Photocatalytic degradation of ciprofloxacin by a novel Z-scheme $CeO_2$-Ag/AgBr photocatalyst: influencing factors, possible degradation pathways, and mechanism insight, J. Catal. 358 (2018) 141–154.

[39] Y. Yang, Z. Zeng, C. Zhang, D. Huang, G. Zeng, R. Xiao, C. Lai, C. Zhou, H. Guo, W. Xue, M. Cheng, W. Wang, J. Wang, Construction of iodine vacancy-rich BiOI/Ag@AgI Z-scheme heterojunction photocatalysts for visible-light-driven tetracycline degradation: transformation pathways and mechanism insight, Chem. Eng. J. 349 (2018) 808–821.

[40] J. Wu, F. Duan, Y. Zheng, Y. Xie, Synthesis of $Bi_2WO_6$ nanoplate-built hierarchical nest-like structures with visible-light-induced photocatalytic activity, J. Phys. Chem. C. 111 (2007) 12866–12871.

[41] J. Zhai, H. Yu, H. Li, L. Sun, K. Zhang, H. Yang, Visible-light photocatalytic activity of graphene oxide-wrapped $Bi_2WO_6$ hierarchical microspheres, Appl. Surf. Sci. 344 (2015) 101–106.

[42] Y. Zou, J.W. Shi, D. Ma, Z. Fan, C. Niu, L. Wang, Fabrication of g-$C_3N_4$/Au/C-$TiO_2$ hollow structure as visibl-light-driven Z-scheme photocatalyst with enhanced photocatalytic $H_2$ evolution, Chemcatchem 9 (2017) 3752–3761.

[43] E. Aguilera-Ruiz, U. García-Pérez, M. Garza-Galván, P. Zambrano-Robledo, B. Bermúdez-Reyes, J. Peral, Efficiency of $Cu_2O/BiVO_4$ particles prepared with a new soft procedure on the degradation of dyes under visible-light irradiation, Appl. Surf. Sci. 328 (2015) 361–367.

[44] D. Huang, Z. Li, G. Zeng, C. Zhou, W. Xue, X. Gong, X. Yan, S. Chen, W. Wang, M. Cheng, Megamerger in photocatalytic field: 2D g-$C_3N_4$ nanosheets serve as support of 0D nanomaterials for improving photocatalytic performance, Appl. Catal., B 240 (2019) 153–173.